



**Transient Photocurrents on Catalyst-Modified n-Si
Photoelectrodes: Insight from Dual-Working Electrode
Photoelectrochemistry**

| | |
|-------------------------------|--|
| Journal: | <i>Sustainable Energy & Fuels</i> |
| Manuscript ID | SE-ART-04-2018-000187.R1 |
| Article Type: | Paper |
| Date Submitted by the Author: | 30-May-2018 |
| Complete List of Authors: | Laskowski, Forrest; University of Oregon, Chemistry Qiu, Jingjing; University of Oregon, Chemistry and Biochemistry Nellist, Mike; University of Oregon Oener, Sebastian; University of Oregon Gordon, Adrian; University of Oregon, Chemistry and Biochemistry Boettcher, Shannon; University of Oregon, |
| | |

Transient Photocurrents on Catalyst-Modified n-Si Photoelectrodes: Insight from Dual-Working Electrode Photoelectrochemistry

Forrest A. L. Laskowski, Jingjing Qiu, Michael R. Nellist, Sebastian Z. Oener, Adrian M. Gordon,
Shannon W. Boettcher*

Abstract

Semiconductor photoelectrodes coated with electrocatalysts are an important component of water-splitting cells that convert and store solar energy. Surface states on light-absorbing semiconductors can function as recombination centers and lower the performance of water-splitting systems. To characterize the presence and impact of surface states on catalyst-coated semiconductors, transient photoelectrochemical behavior is often studied. These experiments typically assume that the filling/emptying of surface states at the semiconductor interface causes transients to occur whenever the incident illumination intensity is perturbed. Analyzing transients may then reveal the density of surface states and their effect on carrier recombination. However, the transient technique does not directly measure the origin of the transient behavior, and utility of the experiment requires assuming an underlying process. Here, we use a dual-working-electrode technique applied to Ni-protected n-Si photoanodes coated with Ni(Fe) (oxy)hydroxide catalyst to examine transient behavior of catalyst-coated photoelectrodes. We find that the most pronounced transients are due to catalyst redox activity. By directly measuring the catalyst redox state, we confirm that transients are related to either catalyst oxidation to Ni(Fe) oxyhydroxide or reduction to Ni(Fe) hydroxide. We also find that the redox-active catalyst moderates how quickly the depletion region and Helmholtz electrostatic potentials relax after each illumination perturbation. The results indicate that a redox-active catalyst can serve as a “parallel capacitor” which influences both the decay time and shape of transients. This data shows that photocurrent transients on catalyzed photoanodes are influenced by the catalyst’s redox-activity and are not solely based on surface state loading/emptying.

1. Introduction

Photoelectrochemical water splitting, achieved by integrating a photocathode and photoanode, converts and stores solar energy in the form of hydrogen fuel.¹ Integrated systems absorb sunlight and use the photo-generated carriers to drive the oxygen evolution (OER) and hydrogen evolution (HER) reactions, simultaneously. However, various processes limit efficiency, especially for the photoanode. The presence of surface states on semiconductors has been shown to increase carrier recombination, thereby decreasing conversion efficiencies.²⁻¹³ To enhance performance, photoanodes are often functionalized with a catalyst which is thought to suppress surface recombination,¹⁴⁻¹⁶ improve OER kinetics,^{17, 18} and/or improve the carrier-selectivity of the interface (e.g. increase band bending).^{19, 20} Some have attributed catalyst enhancement more specifically to the passivation of surface states.^{21, 22} To quantify the impacts of surface states, transient photocurrent analysis has been often applied to understand catalyst-coated photoanodes.^{9, 23}

Transient photocurrent analysis interprets the dynamic response of a photoelectrode as the incident light intensity is modulated.²⁴⁻²⁶ In a typical experiment, current response is collected as an incident light source is periodically switched on and off. Current spikes which rapidly decay to a steady-state value, termed transients, often occur directly after each switch. Transients are thought to be the sum of short-term non-faradaic processes and the steady-state faradaic current (e.g. OER, HER).²⁷⁻³² The exact nature of the non-faradaic processes is system dependent and, for some systems, subject to on-going debate. However, the non-faradaic responses are typically attributed to charge accumulation in the semiconductor depletion region, in the Helmholtz double-layer, or at surface states.^{9, 13, 23, 29, 33-44} For systems where the precise mechanism is deduced, integration of the current-time transient trace is used to characterize the magnitude of charge accumulation.^{9, 45-48} Fitting transient decays, and extracting time constants, has been used to characterize the apparent lifetime of the photogenerated “carriers” (presumably at surface sites) and decay times (from peak to steady-state) have been used to differentiate between plausible decay mechanisms.^{30, 38, 47, 49-51}

Application of transient photocurrent analysis to catalyzed photoanodes has produced diverse results. For Fe_2O_3 photoanodes decorated with cobalt oxyhydroxide phosphate (Co-Pi) catalyst, numerous studies have concluded that the presence of the catalyst increases both the integrated charge in the transient and its amplitude relative to bare photoanodes.^{20, 23, 52-55} Others have found that Co-Pi catalysts suppress the integrated charge in the transient when applied to Fe_2O_3 .^{9, 56} One study found that Co-Pi application yields smaller but broader transients.⁵⁷ Application of Ni- and Ir-based catalysts has been reported to increase the integrated charge in the transient while a report on a Fe-based catalyst found that transients were suppressed.^{32, 50, 58-60} Reports on a “carbon-dot” catalyst and a sub-monolayer Co oxyhydroxide catalyst both found no impact on Fe_2O_3 transients.^{61, 62} For BiVO_4 photoanodes, Co-Pi and Ru-based catalysts have been shown to result in more pronounced transients with increased integration.^{21, 63} But others have found that Co-Pi catalysts and In_2O_3 coatings suppress transients on BiVO_4 .⁶⁴⁻⁶⁸ Meanwhile, reports on Ta_3N_5 photoanodes suggest that IrO_2 catalysts suppress transients while Ni- and Fe-based catalysts significantly increase them.⁶⁹⁻⁷¹ Reports on organic-sensitized photoanodes have shown that Ir-based catalysts decrease both the integrated charge in the transient and the transient amplitude relative to non-catalyzed photoanodes.^{72, 73}

The extent of diverse results has led to a variety of fundamental explanations. In explaining increased amplitude and charge integral of transients, some studies have found that the integrated charge in the transient increases as a function of catalyst loading.^{23, 50, 52, 55} They suggest that on-transients represent catalyst oxidation and off-transients represent reduction. More general hypotheses suggest that recombination pathways are introduced by catalyst deposition.^{54, 74} This has been attributed to the catalyst creating more surface states which increases recombination, or to the catalyst simply increasing the surface capacitance.^{53, 58} A related explanation suggests that catalysts can function as hole storage layers which increases charge integration of transients by promoting recombination with conduction-band electrons.^{32, 71} One study suggested that slower transient decay times represent longer lifetimes for photogenerated charges.²¹ Explanations for transient suppression generally suggest that the catalyst reduces recombination. It has been concluded that catalysts may reduce recombination within the

depletion region, although the mechanism by which this would occur is unclear.⁶⁵ Others report that transients represent surface-state recombination and that catalysts act to “deload” the surface states before recombination can occur.^{48, 59, 68} Decreased transients have also been attributed to general suppression of recombination at the semiconductor/liquid interface.⁷⁵ Still others have suggested that transients represent charge build up at the semiconductor/liquid interface or in surface states; the catalyst acts to consume this charge instead of allowing build-up.^{69, 76} We note that many of these explanations could occur simultaneously; for instance, application of a catalyst could increase surface capacitance while simultaneously passivating surface states.

To better understand photocurrent transients on catalyst-coated semiconductor photoelectrodes we employ a well-defined Si-based model system.⁷⁷ Since Si self-passivates under OER conditions when making solution contact, we use a Ni protection layer which also acts as the catalyst once oxidized.^{74, 78} An advantage in examining this system is that the surface state density on Si is thought to be significantly smaller than either Fe₂O₃ or BiVO₄.^{22, 79-84} Since the Si surface must be buried under the protection layer, it is unlikely that Si|Ni interface states are affected during experiments where additional catalyst is electrodeposited. Thus, we assume that defect-state related charging effects are minor by comparison to other systems. The Si photoanodes protected by a conformal protection layer, are also amenable to the dual-working-electrode (DWE) photoelectrochemical technique.^{85, 86} In this technique an electrolyte-permeable Au contact, deposited on the catalyst surface, is used to sense or control the catalyst potential. We employ the DWE technique to directly measure the electrochemical potential of a Ni-based catalyst during transient experiments. We find that transients are most pronounced in the potential region where illumination changes lead to catalyst redox transitions (as measured by the secondary electrode). The integrated charge of the transients in this potential region is larger than that at other potentials. We also find that the transient shape is influenced by the extent of catalyst loading. Since the rectifying junction is buried under a protection layer (and thereby unaffected by additional catalyst loading), this finding suggests that the redox-active catalyst acts as a capacitor which slows the photoanodes transition to

steady-state after each illumination change. Based on these results we discuss the impacts of redox-active catalysts on interpretation of photocurrent transients.

2. Experimental

2.1 Photoanode fabrication and electrochemical characterization

The fabrication of photoanodes closely followed the preparation described in our previous work.⁷⁷ P-doped [100] n-Si wafers (resistivity 0.65-0.95 ohm·cm) were diced into 1 × 1 cm squares and sonicated for 10 min in acetone (99.8%, Fisher Chemical), iso-propyl alcohol (99.9%, Fisher Chemical) and nanopure water (18.2 MΩ). Diced squares were then cleaned for 30 min in boiling Piranha (3:1 by volume H₂SO₄ : H₂O₂, 100 °C, both procured from Fisher Chemical), rinsed twice and dried under filtered N₂ (0.01 micron – McMaster-Carr). The Ni protection layer and catalyst were deposited without removing the native oxide via electron beam evaporation (Amod evaporation system) at $\sim 0.1 \text{ \AA s}^{-1}$ from a Fabmate crucible (Kurt Lesker) packed with Ni pellets (Kurt Lesker, 1/4" diameter & 1/2" length, 99.995%). In a typical deposition, 5 nm of Ni metal was deposited; this produces lower performing photoanodes (decreased photovoltage) relative to our previous work but ensures photoanode longevity and protects against shorting during deposition of the second working electrode Au top contact.⁷⁷ An ohmic back contact was achieved by scratching through the native oxide on the backside of the n-Si, wetting with Ga-In eutectic ($\geq 99.99\%$, Sigma Aldrich), and then affixing a Sn-Cu wire (30 AWG) within the eutectic. The Sn-Cu wire was affixed via hot glue and threaded through a 3.5 mm-diameter glass tube which serves as the electrode stem. The backside of the Si and the Sn-Cu wire were then sealed with epoxy (Loctite Hysol 1C) to prevent solution contact.

Before additional fabrication steps, the electrodes were activated by cycling 50 times at 100 mV s⁻¹ in 1 M potassium borate buffer at pH 9.5 (K-borate). Cycles were performed under ~ 1 sun AM1.5G illumination (Abet Technologies, model 10500) in a potential window with endpoints 200 mV cathodic of the Ni reduction peak and 200 mV anodic of the Ni oxidation peak. This process converts a portion of the Ni protection layer to an active Ni(Fe)(OH)₂/Ni(Fe)OOH catalyst. To examine the impacts of catalyst loading, additional Ni(Fe)OOH

was electrochemically photodeposited by saturating the buffer with NiCl₂ (calculated to 0.1 M NiCl₂) and then continuing the illuminated cycling (15-30 additional cycles). We note that unintentional trace Fe cations incorporate into the catalyst, but since this is not the focus of the present work we will hereafter refer to the catalyst as Ni(OH)₂/NiOOH.⁸⁷⁻⁸⁹

The secondary working electrode was deposited in one of two ways, depending on the intended experimental purpose. To sense the catalyst electrochemical potential, 10 nm of Au was thermally deposited directly after the electrochemical Ni (oxy)hydroxide deposition. This ensures that the Au does not short to the metallic Ni protection layer and only senses the redox-active catalyst. To sense the Ni protection layer electrochemical potential, the 10 nm of Au were thermally deposited directly prior to electrochemical NiOOH deposition. The difference between these two configurations is reflected in the data obtained from the second working electrode (WE₂). The data is either characteristic of conductivity transitions when sensing the catalyst electrochemical potential (Ni (oxy)hydroxide is only conductive when oxidized) or depicts conductive behavior irrespective of applied potential when sensing the metallic Ni protection layer electrochemical potential.⁸⁹ In both cases, the Au was thermally deposited at $\sim 2 \text{ \AA s}^{-1}$ from an alumina-coated boat (Kurt Lesker). A schematic depiction of the two different DWE deposition strategies can be found in Figure S1.

Electrodes were electrochemically characterized in 50 mL of aq. 1 M K-borate buffer (pH ~ 9.5) using a BioLogic SP200 bipotentiostat. All experiments were performed with a Pt counter electrode and either a Ag/AgCl or Hg/HgO reference electrode. Cyclic voltammograms were not corrected for uncompensated series resistance. For transient experiments the photoanode was poised at various applied potentials while the light was manually switched off/on each minute. Three off-transients and three on-transients were collected at each applied potential. All experiments were performed with mild stirring to dislodge any O₂ bubbles formed. At least three electrodes were examined for each experiment described below; a single representative electrode is selected for explanation of the results. All the potentials are referenced to $\varepsilon_{\text{O}_2/\text{OH}^-}$ according to the following equation:

$$V \left(v.s. \varepsilon_{\frac{\text{O}_2}{\text{OH}^-}} \right) = V_{\text{experimental}} (v.s. \varepsilon_{\text{reference}}) + \varepsilon_{\text{reference}} (v.s. \text{SHE}) + 0.059 \text{ V} * \text{pH} - 1.23 \text{ V}$$

3. Results & Discussion

3.1 Effects of catalyst loading on transient photocurrent response

To understand if redox-active catalysts influence photocurrent transients, we first examined Ni-protected n-Si photoanodes with varied catalyst loadings. For these devices we iterated between collecting illuminated cyclic voltammograms (CVs), collecting photocurrent transient data, and photo-depositing additional redox-active Ni (oxy)hydroxide. Photodeposition was performed by sweeping 15 CVs, under illumination, in a NiCl₂-saturated solution as described in the experimental section. To quantify the extent of redox-active Ni (oxy)hydroxide present, the cathodic redox peak from each CV (corresponding to Ni (oxy)hydroxide reduction) was integrated (Figure 1).

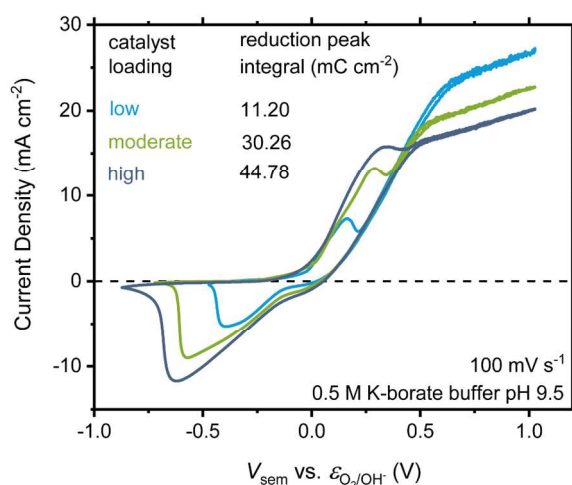


Figure 1. Illuminated voltammetry collected after each transient experiment as a function of photodeposited catalyst loading. All experiments were performed on the same electrode where catalyst loading (low, moderate, high) was increased after each transient experiment (immediately after the CVs shown here). The inset shows the results of the integration of the cathodic redox peak, which is proportional to the number of redox-active Ni sites in the catalyst layer. The data shows the extent of redox-active catalyst present during each transient experiment.

Transients are first collected with the semiconductor photoelectrode poised at an applied potential $V_{\text{sem}} = -0.2$ V vs. the thermodynamic potential for water oxidation ($\epsilon_{\text{O}_2/\text{OH}^-}$) and then at each 25 mV

increment as the photoelectrode is stepped 600 mV anodic of the starting potential (Figure 2). The photoanode is held at each potential step for 7 min, during which time the light is switched off at the beginning of each odd numbered minute and on at the beginning of each even numbered minute. Anodic and cathodic transients exist over the entire applied potential range. However, integration of the current transients reveals a potential region (>250 mV), for each experiment, where transient integrated charge is increased. As additional catalyst is photodeposited, the region of increased integrated charge shifts cathodic and the integrated charge increases.

The region of increased integrated charge can be attributed to oxidation/reduction of the Ni catalyst. This conclusion is supported by comparing the integrated charge for each photo-deposition step (Figure S2). As more catalyst is photodeposited, the integrated charge in the voltammetry (Figure 1) and the transient (Figure 2) increase together. Since the semiconductor surface remains buried under the protection layer during each catalyst deposition, this behavior cannot be due to changes in interface state density. The cathodic shift of the region of increased integrated charge is attributed to an increase in the photovoltage as the photoelectrode ages (Figure 2 and Figure S3). The ageing phenomenon, explained in our previous work, relates to the protection layer becoming increasingly electrolyte permeable.⁷⁷ This explanation is consistent with the anodic shift in OER onset seen when comparing voltammograms immediately before and after the first transient experiment (Figure S3). The data in this section thus shows that (1) the catalyst layer affects the transient response, (2) the effect is most pronounced in the region of increased integrated transient charge, and (3) that higher loading of catalyst yields larger integrated charge in the transients.

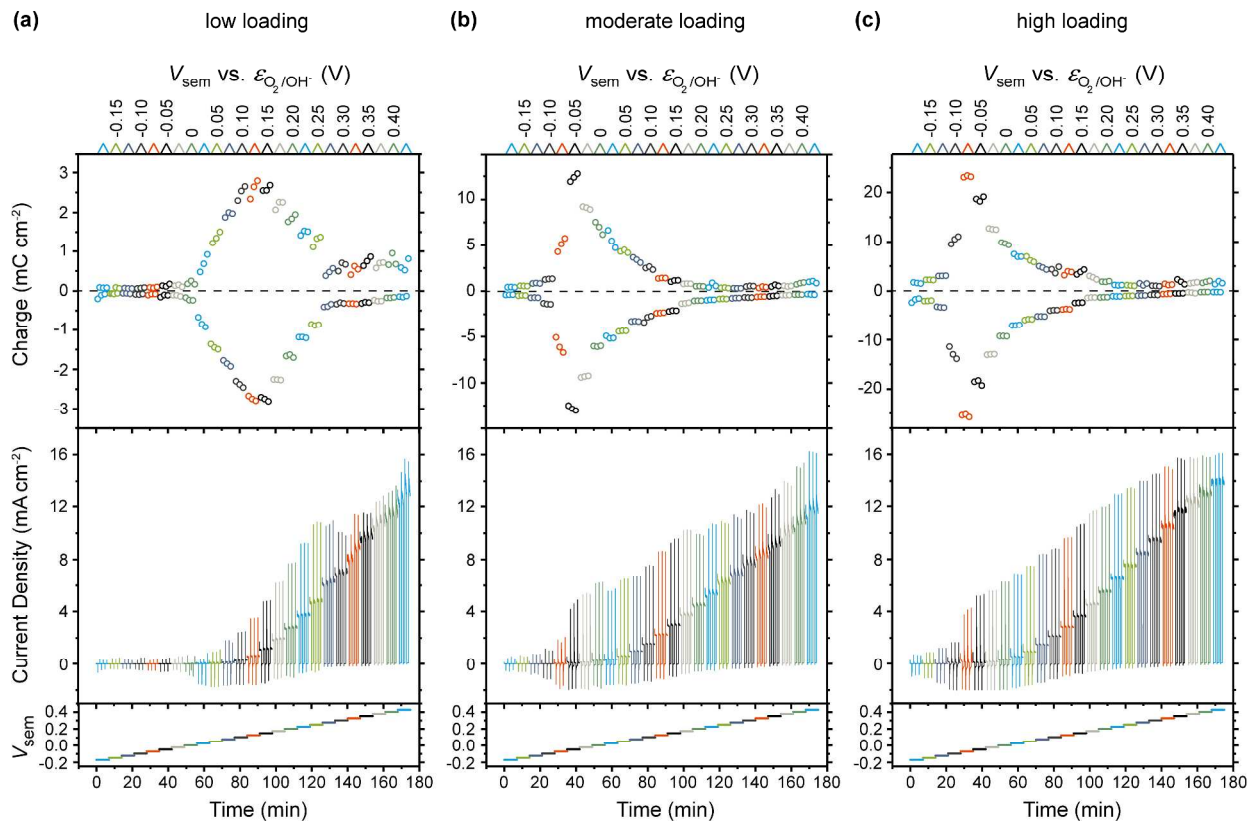


Figure 2. Transient response as a function of catalyst loading. The bottom pane shows V_{sem} vs. $\epsilon_{\text{O}_2/\text{OH}^-}$ as a function of time. The middle pane depicts the transient photocurrent response collected every 1 ms. The top pane depicts the integration of the transients which reveals a >250 mV range where integrated charge is most prominent. The dependence on V_{sem} is also depicted along the top x-axis for each figure. Comparison between the different extents of catalyst loading: **(a)** low, **(b)** moderate, and **(c)** high, shows that increased loading produces larger integrated charge in the transients.

3.2 Dual-working-electrode measurements of catalyst potential during photocurrent transients

To directly measure the catalyst behavior during transient experiments, the dual-working-electrode (DWE) photoelectrochemistry technique was used. In these experiments, the first working electrode (WE_1) was attached to an ohmic contact on the backside of the n-Si semiconductor and the second working electrode (WE_2) was attached to a thin electrolyte-permeable Au top-contact (see Figure S1 for additional details). The Au layer was evaporated onto the photoanode after both activation and additional Ni (oxy)hydroxide had been photodeposited. Due to the fragile nature of this secondary contact

(it tends to be exfoliated by prolonged oxygen evolution), WE_1 is stepped in 100 mV increments instead of 25 mV increments. Data is collected every 100 ms to accentuate the region of increased integrated transient charge. Illumination chopping periodicity and all other experimental parameters remain the same as in Section 3.1. During each experiment the current density at WE_1 (J_{sem}) and the voltage at WE_2 (V_{cat}) are simultaneously recorded (Figure 3).

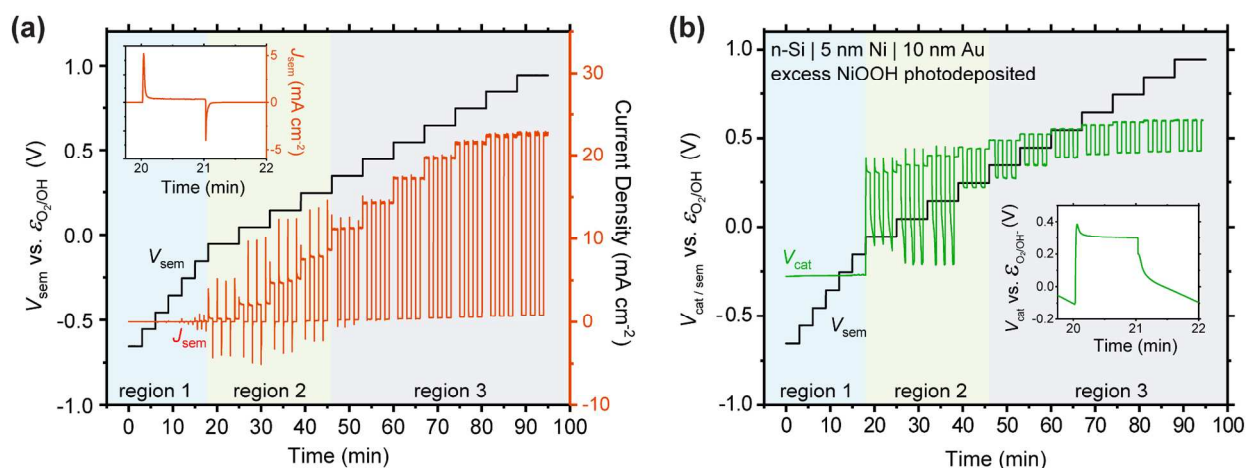


Figure 3. Measurement of catalyst potential during transient experiments. Three light-on/light-off transient sets were recorded for each potential (V_{sem}) step. Three regions of activity are denoted (discussed in the main text) on each panel. **(a)** Transient J_{sem} response (red) as a function of time and hence WE_1 applied potential (V_{sem}). Transients are only apparent in region 2. **(b)** V_{cat} (WE_2) response (green) for the same transients. When the light is turned off, two regions of V_{cat} decay (panel b) are exhibited in region 2: a quick decay followed by a slower decay which fails to reach a steady-state value before the light is turned back on. Insets in both panels show one set of transients in region 2. The data shows that the catalyst potential V_{cat} , for regions 2 and 3, varies in tandem with the transient photocurrent response – i.e. during on-transients the catalyst is oxidized and during off-transients the catalyst is reduced.

The chopped illumination data exhibits three regions of distinct transient behavior (Figure 3). In the first region, corresponding to the first six V_{sem} voltage steps (-0.65 to -0.15 V vs. ϵ_{O_2/OH^-}), transients are absent or very small. The catalyst potential, V_{cat} , measured via WE_2 and the semiconductor current density, J_{sem} , remain constant in this region (Figures 3a and 3b); i.e. J_{sem} and V_{cat} are nonresponsive to both the applied V_{sem} and to changes in the illumination condition. Catalyst voltammograms (collected via

WE₂ directly after transient experiments, see Figure S4) show that the onset of catalyst oxidation occurs at ~ 0.3 V vs. $\epsilon_{\text{O}_2/\text{OH}^-}$. Because V_{cat} remains near -0.3 V vs. $\epsilon_{\text{O}_2/\text{OH}^-}$ throughout region 1 of the transient experiment, the catalyst remains in its non-conductive Ni(OH)₂ state.

In region 2, on- and off-transients are observed for V_{sem} potentials between -0.05 and 0.25 V vs. $\epsilon_{\text{O}_2/\text{OH}^-}$. As the light is turned on both J_{sem} and V_{cat} quickly increase before decaying to a steady-state value (Figure 3a). Integration of the largest J_{sem} on-transient (6.5 mC cm⁻²) compares favorably to integration of the redox wave in the catalyst voltammograms shown in Figure S4 (8 mC cm⁻²). The on-transients thus represent catalyst oxidation in this region. When the light is switched off both J_{sem} and V_{cat} simultaneously decrease. J_{sem} exhibits a negative current transient before decaying back to ~ 0 mA cm⁻².

For many of these electrodes, the magnitudes of the integrated J_{sem} off-transients are ~ 30 % smaller than the integrated on-transients. Additionally, for these electrodes, V_{cat} exhibits a quick initial decay (through the first ~ 200 mV) followed by a much slower decay thereafter (Figure 3b - inset). These two findings are explained as follows. When the light turns off the hole population collapses and hole quasi-Fermi level returns to the majority electron Fermi level. Electrons are then transferred from the conduction band to the catalyst directly in contact with the semiconductor, reducing NiOOH to Ni(OH)₂. Because Ni(OH)₂ is an electronic insulator, reduction of the near-surface NiOOH may electronically isolate regions of the catalyst further from the semiconductor|catalyst interface. For these isolated catalyst areas, the catalyst cannot be re-reduced from the semiconductor and thus the oxidized state must relax via a slower equilibrium with the solution (i.e. to discharge and generate oxygen gas). Hence the light-off V_{cat} response is characterized by a quick decay followed by a slow decay (Figure 3b - inset). This picture is supported by the fact that the slow V_{cat} decay occurs after J_{sem} has reached its dark steady-state value (~ 0 mA cm⁻²).

In Region 3 ($V_{\text{sem}} = 0.35 - 0.95$ V vs. $\epsilon_{\text{O}_2/\text{OH}^-}$), no transients are observed. However, unlike region 1, both J_{sem} and V_{cat} are responsive to the light condition. As the light is turned on, J_{sem} and V_{cat} simultaneously increase and achieve a steady-state. When the light is turned off they each relax to

respective lower values and achieve a new steady-state. The fact that V_{cat} reaches steady-state in the dark demonstrates that the catalyst remains oxidized and that WE_2 is in electronic contact with the semiconductor. This is further evidenced by the lack of a second slower V_{cat} decay, and the lack of the J_{sem} on/off-transients. We also note that, in Region 3, V_{cat} remains positive of ~ 0.3 V vs $\epsilon_{\text{O}_2/\text{OH}^-}$ (the oxidation onset potential measured for the catalyst alone, see Figure S4). This data indicates that the surface-majority-carrier Fermi level is no longer capable of reducing the catalyst in the dark. Instead, the small leakage current from the semiconductor is sufficient to keep the catalyst oxidized. During light-on, V_{cat} increases but no redox transition occurs.

The data presented above for regions 1, 2 and 3 indicate that a significant transient response only occurs when the dark-to-light range of V_{cat} (ΔV_{cat}) overlaps the catalyst's redox-active potential range. The catalyst's redox activity range can be measured directly using WE_2 for the same device on which transients are measured. For the device in Figure 3 the onset of catalyst reduction occurs at ~ 0.25 V vs. $\epsilon_{\text{O}_2/\text{OH}^-}$ and the onset of oxidation occurs at ~ 0.3 V vs. $\epsilon_{\text{O}_2/\text{OH}^-}$ (Figure S4). For regions 1 and 3, the measured V_{cat} remains below or above this redox activity range, respectively (Figure 3b). However, for region 2 where transients are most pronounced, V_{cat} transitions through the redox range immediately following each light switch. This directly shows that the most pronounced transient behavior is associated with the oxidation and reduction of the catalyst. The appearance of transients is an indication that ΔV_{cat} is partially or fully eclipsing the range of catalyst redox activity.

To help explain this finding, band diagrams for the processes occurring in region 2 are depicted in Figure 4. In the dark, the applied potential is such that the majority carrier Fermi level ($E_{\text{f,n}}$) rests cathodic of the catalyst's redox-activity region. Once illuminated, the generated minority-carrier profile results in a photovoltage which drives the oxidation of the catalyst. Charge accumulation at the solution interface pushes the protection-layer Fermi level (E_{Ni}) through the region of catalyst redox activity. The catalyst Fermi level (E_{cat}) remains in quasi-equilibrium with the protection layer and this results in the catalyst oxidation. Removal of the light source leads to re-reduction of the catalyst as the hole quasi-Fermi-level

($E_{f,p}$) equalizes with $E_{f,n}$. Thus, the transient behavior depicted in region 2 occurs as a function of the applied potential and the photovoltage. Significant transients occur whenever the applied V_{sem} places $E_{f,n}$ cathodic of the redox activity region in the dark and the photovoltage is sufficiently large such that the photogenerated holes can drive catalyst oxidation in the light.

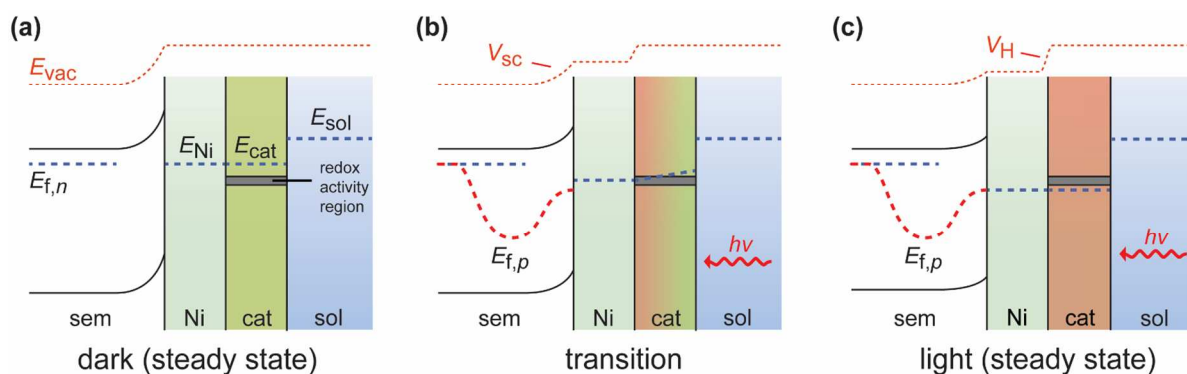


Figure 4. Schematic band diagrams of transition of system between dark and light states. The figure represents the typical case for transient experiments where the applied V_{sem} is anodic of the equilibrium solution potential (here set by $\varepsilon_{O_2/OH^-} = E_{sol}/q$). The green catalyst represents the electrolyte permeable $Ni(OH)_2$ while the red catalyst represents $NiOOH$. The transition behavior (panel b) depicts a gradient in redox states that may occur as the catalyst transitions from $Ni(OH)_2$ to $NiOOH$. The semiconductor, metallic Ni protection layer, redox-active catalyst and solution are represented by sem, Ni, cat, and sol, respectively. E_{Ni} , E_{cat} , and E_{sol} represent the electrochemical potential for the protection layer, catalyst, and solution, respectively. The quasi-Fermi levels are depicted by $E_{f,n}$ and $E_{f,p}$. A redox activity region (gray box) represents a catalyst “redox density of states (DOS)” which are filled/emptied during redox transitions. The vacuum level, represented by E_{vac} , is shown as modified by the electrostatic potential. V_{sc} and V_H represent the depletion-region electrostatic potential and Helmholtz electrostatic potential, respectively. We note here that V_H is truly assigned at the Ni|solution interface, which is proximal to the Ni|catalyst interface only because the catalyst is electrolyte permeable. During transient experiments ΔV_{sc} must equal $-\Delta V_H$ to maintain E_{sem} fixed versus E_{sol} , as is controlled by the potentiostat (the difference between the reference electrode potential and solution potential is fixed). For region 2, the dark majority carrier level is sufficiently cathodic to reduce the catalyst (panel a). Once illuminated, holes arriving at the solution interface force an increase in V_H which eventually moves E_{Ni} to the redox activity region (panel b). E_{cat} maintains quasi-equilibrium with E_{Ni} and this causes oxidation of the catalyst (panel c). The temporal transition to the illuminated steady-state is slowed by the catalyst layer because holes that would be contributing to increasing V_H are now partially being consumed for catalyst redox chemistry. Since $\Delta V_{sc} = -\Delta V_H$, the band unbending is also slowed, and the transient photocurrent response is characterized by larger currents over a longer duration.

3.3 Dual-working-electrode measurements of the protection-layer potential during photocurrent transients

We next consider the shape of the transient responses and explain it in terms of a band picture. We make measurements on electrodes where the thin electrolyte-permeable Au layer is deposited after photoanode activation, but before additional NiOOH catalyst is photodeposited onto the surface. This results in contact between the Au WE₂ and the Ni metallic protection layer, as can be seen by the fact that V_{cat} is now responsive to light on/off cycles at all potentials (Figure S5); i.e. the measurement is not limited by the insulating nature of the reduced Ni(OH)₂ form of the catalyst. Measuring the surface potential does not require that the catalyst is in an electrically conductive state. Instead of sensing the redox-active catalyst electrochemical potential, the contact now equilibrates with the protection layer electrochemical potential. Since the protection layer consists of dense metallic Ni, during transients its electrochemical potential can only be modified by charge built-up at the metal|solution interface (the catalyst layer is permeable to electrolyte). Thus, by observing the protection layer electrochemical potential we sense changes to the Helmholtz electrostatic potential (shown in Figure 4c).

Figure 5 shows cathodic J_{sem} transients and the associated V_{Ni} response for a device with the second working electrode attached directly to the metallic Ni protection layer. Transient integrated charge and the complete J_{sem} and V_{Ni} dataset can be found in Figure S5. We select five of the cathodic transients to examine in more detail. Figure 5a depicts a cathodic transient from region 1, i.e. at V_{sem} cathodic of the catalyst redox activity. Transients shown in Figure 5b, 5c, and 5d are from region 2, in order of increasing anodic applied potentials. The transient shown in Figure 5e is from region 3, at V_{sem} anodic of the catalyst redox potential region. When the catalyst redox activity is not present (regions 1 and 3), the current transient completely decays to steady-state within 1 s (Figure 5a and 5e). The V_{Ni} response mirrors the decay time and the decay shape. For the transients in Figure 5b and 5c, the photocurrent decays over a much longer timeframe (> 5 s) and deviates from the visibly exponential shape of those in Figure 5a and 5e. The exponential current decay to steady-state is interrupted by a region of more moderate decay (diminished slope). V_{Ni} decays over the same timeframe and visibly mirrors the shape of the current

decay. Finally, the transient in Figure 5d lacks the complex shape of the previous two, but decays over a longer timeframe than either transient in Figure 5a or 5e. All three transients selected from region 2 show significantly slower decay times and exhibit V_{Ni} responses which mirror the J_{sem} decay shape.

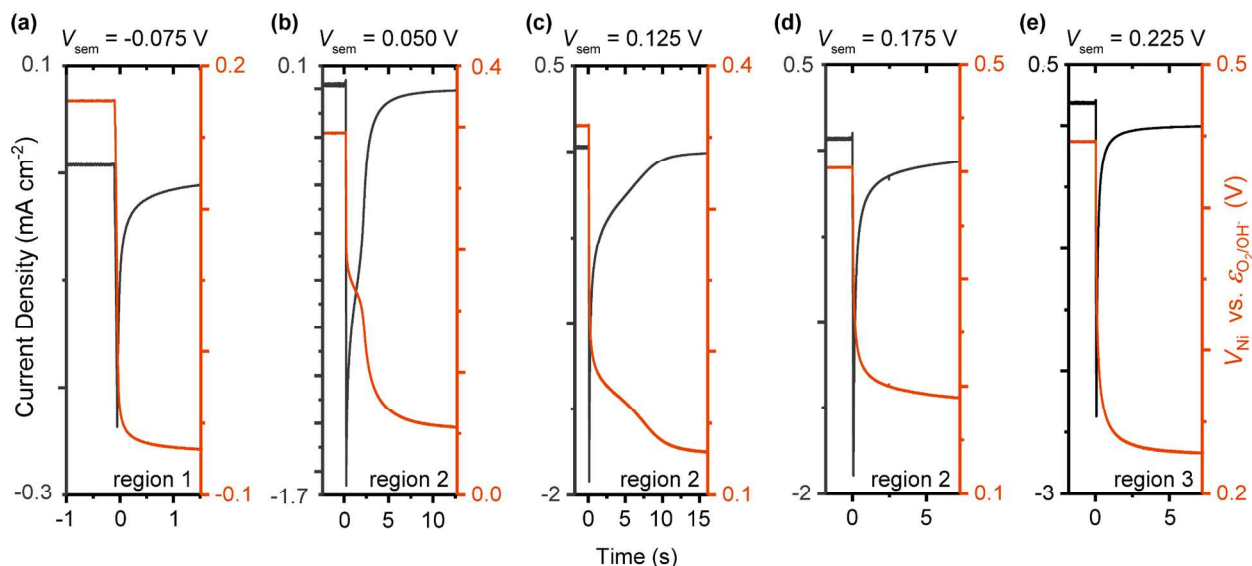


Figure 5. Sensing the protection layer electrochemical potential. The results depict J_{sem} and V_{Ni} from five representative transients as sensed via WE₁ and WE₂, respectively. Panel (a) shows a transient from region 1. Panels (b), (c) and (d) show transients from region 2 in order of increasingly anodic applied potential. Panel (e) shows a transient in region 3. This data shows that when the off-transient causes V_{Ni} to traverse the onset of catalyst reduction (at ~ 0.20 vs $\epsilon_{\text{O}_2/\text{OH}^-}$) the decay in the protection layer electrochemical potential is slowed (Figure S6). The decay shape for J_{sem} becomes visibly more complex and this shape is mirrored by the V_{Ni} decay.

The above results indicate that the redox-active Ni (oxy)hydroxide catalyst acts as a “capacitor” which moderates how quickly the semiconductor depletion region and Helmholtz electrostatic potentials relax when moving from light to dark. For the transients in Figure 5b and 5c, V_{Ni} collapses quickly in each case until it reaches ~ 0.2 V vs. $\epsilon_{\text{O}_2/\text{OH}^-}$. This potential is consistent with where the redox-active catalyst is converted from NiOOH to Ni(OH)₂, and so it represents the edge of the catalyst’s “redox density of states (DoS)” (Figure S6a). Once the Helmholtz potential has decayed to place E_{Ni} near the catalyst reduction onset, electrons injected from the conduction band can reduce the catalyst, in addition

to accumulating at the Ni|solution interface. If charge is not injected into the catalyst, for example due to slow charge transfer kinetics between Ni and catalyst, the fast exponential decay would continue without any region of slowed transient decay.^{9, 47, 90, 91} However, the data above shows that the decay is slowed, indicating that charges are injected into the catalyst once V_H has sufficiently relaxed.

The potential range for the more moderate slope in region 2 of the transient decays is associated with the catalyst's redox DoS. In the Figure 5b transient, the "diminished" V_{Ni} decay occurs through a ~40 mV range, while for the Figure 5c transient the "diminished" decay occurs through a ~38 mV range. This data suggests that the catalyst contains a redox DoS spanning 38-40 mV, which is consistent the redox peak widths from WE_2 voltammetry collected at 1 mV s^{-1} (Figure S6b). Once the Helmholtz electrostatic potential aligns E_{Ni} with the edge of this 38-40 mV region, the redox states begin to compete for consumption of injected electrons; any change in the Helmholtz electrostatic potential must correlate with the same potential change in the catalyst redox DoS. Upon filling the catalyst DoS the catalyst "parallel capacitance" vanishes, and current/voltage decay can once again continue exponentially. This final point is experimentally supported by the resumed rapid V_{Ni} decay after the 38-40 mV have transpired (Figures 5b and 5c).

For further evidence that the catalyst redox DoS moderates the transient photocurrent/photovoltage decay we return to the loading dependence data from Section 3.1. In Figure 6a all three transient loadings are compared at a constant applied potential near the OER onset. To account for shifts in the transient integration region due to different photovoltages provided by the rectifying junction, in Figure 6b the transients which exhibit maximum charge integration at each loading are also compared. In both cases, increased loading produces not only an increase in the integration of the anodic transient but also a broadened transient decay shape. The cathodic transients exhibit more-exponential behavior but their decay to zero current is also broadened as loading increases. The cathodic transients at moderate and high catalyst loading fail to reach zero current before the light is switched on again. By contrast, the low loading cathodic transient returns to zero in both examples. These results demonstrate

that larger absolute transient currents are sustained for longer when more catalyst is coated onto the photoanode.

The catalyst loading results can be related to the band-bending model in Figure 4. For the anodic light-on transients, where photocurrent decay is governed by the rate of electrons injected from the conduction band, increased catalyst loading causes the semiconductor bands to unbend more slowly. For the cathodic transients, where decay is related to how quickly the bands regain their dark equilibrium state, increased catalyst loading causes the bands to re-bend over a longer duration. These findings are consistent with the above understanding, where interaction with the catalyst redox states slows how quickly the Helmholtz electrostatic potential responds to changes in the illumination. As the number of catalyst redox states increases the electrostatic potential transition further slows and so the transient relaxation time increases.

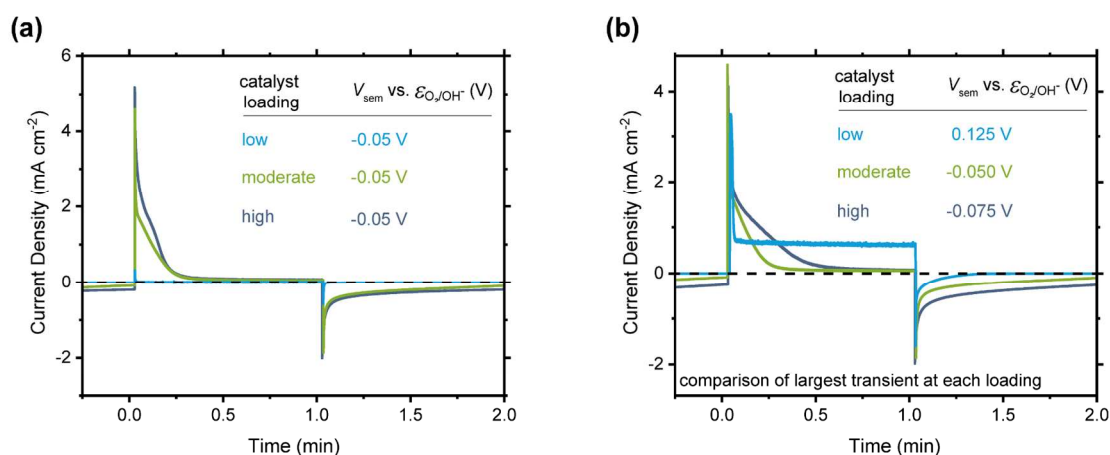


Figure 6. Transients vs. catalyst loading on the same sample shown in Figure 2. One set of on/off transients selected from the overall data. **(a)** All three loadings compared at -50 mV vs. ϵ_{O_2/OH^-} . **(b)** Comparison of the transient with largest charge integration at each catalyst loading extent. The applied potential for each loading is shown in the inset. Increased loading in each case results in broader transient features. Anodic transients exhibit non-exponential decay as loading increases. The results show that increased catalyst loading causes broader transients oftentimes with complex decay shapes.

4. Conclusions

Experiments on Ni-protected n-Si illustrate how photocurrent transients are affected by the presence of a redox-active oxygen evolution catalyst. The application of the catalyst produces three distinct regions of transient activity. At sufficiently low and high applied potentials, only very quick transients appear with relatively small charge integration. Between these two regions of activity exists a region with large charge integration and relatively slow decay times. Here, we find that the integrated charge is related to the quantity of redox-active catalyst on the semiconductor surface. DWE experiments reveal that this behavior takes place when the applied potential is such that: (a) the majority carrier Fermi level can reduce the catalyst in the dark and (b) the minority carrier Fermi level can oxidize the catalyst once illuminated. Since the photovoltage is given by the difference between the two quasi-Fermi levels, photoanodes with greater photovoltages (such as BiVO_4 where the photovoltage is nearly 1 V) are expected to exhibit this behavior over a greater applied potential range.^{92, 93}

The presence of a redox-active catalyst slows the electrostatic relaxation events during transient experiments. This occurs whenever an illumination switch causes the surface electrochemical potential at the protection layer to pass through the catalyst's redox density of states. With little or no catalyst, relaxation is characterized by carriers injected from the semiconductor interacting to increase/decrease the Helmholtz electrostatic potential at the Ni protection layer surface. In the presence of the Ni (oxy)hydroxide catalyst this relaxation process is slowed because some of the carriers are now consumed for catalyst redox activity. A larger catalyst redox density of states promotes this effect, by essentially acting as a larger parallel capacitor, and gives rise to more complex and extended transient decay shapes. This explains, in part, the more complex and/or extended decay shapes that arise after catalyst application in many recent reports on a variety of oxide photoanodes.^{23, 32, 52, 55, 57, 63, 66, 70, 71, 74, 75, 94-96} We note that this behavior is dependent on the catalyst being in quasi-equilibrium with the surface electrochemical potential. For systems without quasi-equilibrium (slow transfer between semiconductor and catalyst), the electrostatic profile may relax before redox activity takes place. One situation where such behavior occurs

is in the re-reduction of the oxidized Ni (oxy)hydroxide catalyst during the off-transient; initial discharge can result in an electrically insulating near-semiconductor layer which prevents complete reduction of the catalyst by electrons from the semiconductor. Similarly, in systems employing the Co-Pi catalyst, lack of cathodic off-transients may be related to slow reduction kinetics.^{16, 23, 64, 76, 95}

The utility of transient photocurrent experiments relies on assigning transients to a specific process. For example, using transient integration to quantify surface states requires attributing the transient response to surface state filling/emptying. However, we show that the Ni-based redox-active catalyst can influence transients, causing increased integrated charge in the transient, extended decay times, and complex decay shapes. The findings and proposed mechanism suggest that this is a general phenomenon for catalysts that exhibit electrochemical redox transitions in the potential range of interest. Catalysts without such redox features prior to the OER onset are not expected to influence transient features in the same way as reported here. These findings have general implications for analyzing photoelectrochemical transients – those on catalyzed systems may represent more processes than the filling/emptying of surface states. If the catalyst's redox DoS overlaps a surface-state DoS then transients are expected to be influenced by both. For these transients, decay time characterization and transient integration describe the conflated relaxation processes and may not accurately depict either isolated process. Additionally, for systems with larger photovoltages than the n-Si studied here (e.g. BiVO₄, Fe₂O₃), we anticipate that this conflated relaxation response occurs over a much greater applied potential range. Comparison of photocurrent transients as a function of catalyst mass loading can be employed to indicate if and where the catalyst is influencing transients. When catalyst influence is present, multi-exponential decay fits may be useful in isolating processes that occur before/after interaction with the catalyst redox DoS. Several groups have reported that single exponential fits are insufficient for fitting decay time constants for catalyzed systems and have relied on multi-exponential fits.^{49, 50, 55} However, for processes occurring at similar time scales, the DWE technique is useful as it provides a direct measure of the catalyst charging. The DWE measurement could be used to separate out the extent of transient behavior due to catalyst charging, relative to that due to surface-state charging.

ASSOCIATED CONTENT

Supporting Information

The Supporting Information is free of charge.

Photoanode fabrication information, additional photoelectrochemical and dual-working-electrode data.

AUTHOR INFORMATION

Corresponding Author

Shannon Boettcher - Department of Chemistry and Biochemistry, University of Oregon, Eugene, Oregon 97403, USA. E-mail: swb@uoregon.edu

Author Contributions

The manuscript was written through contributions of all authors. All authors have given approval to the final version of the manuscript.

ACKNOWLEDGEMENTS

This work was funded by the Department of Energy, Basic Energy Sciences, award number DE-SC0014279. F.A.L.L. acknowledges support from a NSF graduate research fellowship grant, number 1309047. S.W.B acknowledges support from the Sloan and Dreyfus foundations. We acknowledge use of the CAMCOR shared instrumentation, which is supported by grants from the M. J. Murdock Charitable Trust, the W. M. Keck Foundation, ONAMI, and the NSF.

REFERENCES

1. M. G. Walter, E. L. Warren, J. R. McKone, S. W. Boettcher, Q. X. Mi, E. A. Santori and N. S. Lewis, *Chem. Rev.*, 2010, **110**, 6446-6473.
2. S. M. Ahmed, J. Leduc and S. F. Haller, *J. Phys. Chem.*, 1988, **92**, 6655-6660.
3. M. Barroso, C. A. Mesa, S. R. Pendlebury, A. J. Cowan, T. Hisatomi, K. Sivula, M. Gratzel, D. R. Klug and J. R. Durrant, *Proc. Natl. Acad. Sci. U. S. A.*, 2012, **109**, 15640-15645.
4. M. P. Dareedwards, J. B. Goodenough, A. Hamnett and P. R. Trevellick, *J. Chem. Soc., Faraday Trans.*, 1983, **79**, 2027-2041.
5. J. A. Glasscock, P. R. F. Barnes, I. C. Plumb and N. Savvides, *J. Phys. Chem. C*, 2007, **111**, 16477-16488.
6. T. Hisatomi, F. Le Formal, M. Cornuz, J. Brillet, N. Tetreault, K. Sivula and M. Gratzel, *Energy Environ. Sci.*, 2011, **4**, 2512-2515.
7. G. Horowitz, *J. Electroanal. Chem.*, 1983, **159**, 421-436.
8. P. Iwanski, J. S. Curran, W. Gissler and R. Memming, *J. Electrochem. Soc.*, 1981, **128**, 2128-2133.
9. F. Le Formal, K. Sivula and M. Gratzel, *J. Phys. Chem. C*, 2012, **116**, 26707-26720.
10. J. Leduc and S. M. Ahmed, *J. Phys. Chem.*, 1988, **92**, 6661-6665.
11. W. H. Leng, Z. Zhang, J. Q. Zhang and C. N. Cao, *J. Phys. Chem. B*, 2005, **109**, 15008-15023.
12. C. Sanchez, K. D. Sieber and G. A. Somorjai, *J. Electroanal. Chem.*, 1988, **252**, 269-290.
13. O. Zandi and T. W. Hamann, *J. Phys. Chem. Lett.*, 2014, **5**, 1522-1526.
14. J. E. Thorne, J. W. Jang, E. Y. Liu and D. W. Wang, *Chem. Sci.*, 2016, **7**, 3347-3354.
15. D. K. Zhong, S. Choi and D. R. Gamelin, *J. Am. Chem. Soc.*, 2011, **133**, 18370-18377.
16. C. Zachäus, F. F. Abdi, L. M. Peter and R. Van De Krol, *Chem. Sci.*, 2017, **8**, 3712-3719.
17. G. M. Carroll, D. K. Zhong and D. R. Gamelin, *Energy Environ. Sci.*, 2015, **8**, 577-584.
18. D. K. Zhong and D. R. Gamelin, *J. Am. Chem. Soc.*, 2010, **132**, 4202-4207.
19. M. Barroso, A. J. Cowan, S. R. Pendlebury, M. Gratzel, D. R. Klug and J. R. Durrant, *J. Am. Chem. Soc.*, 2011, **133**, 14868-14871.
20. D. R. Gamelin, *Nat. Chem.*, 2012, **4**, 965-967.
21. M. de Respinis, K. S. Joya, H. J. M. De Groot, F. D'Souza, W. A. Smith, R. van de Krol and B. Dam, *J. Phys. Chem. C*, 2015, **119**, 7275-7281.
22. R. Liu, Z. Zheng, J. Spurgeon and X. G. Yang, *Energy Environ. Sci.*, 2014, **7**, 2504-2517.
23. B. Klahr, S. Gimenez, F. Fabregat-Santiago, J. Bisquert and T. W. Hamann, *J. Am. Chem. Soc.*, 2012, **134**, 16693-16700.
24. L. M. Peter, *Chem. Rev.*, 1990, **90**, 753-769.

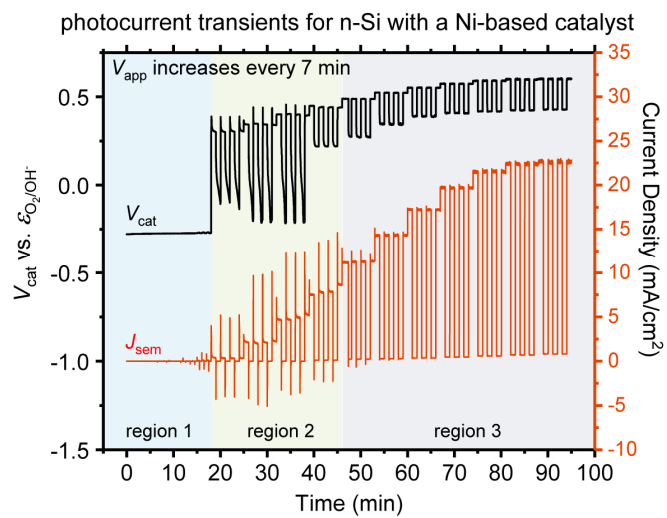
25. L. Steier, I. Herraiz-Cardona, S. Gimenez, F. Fabregat-Santiago, J. Bisquert, S. D. Tilley and M. Gratzel, *Adv. Funct. Mater.*, 2014, **24**, 7681-7688.
26. A. G. Tamirat, J. Rick, A. A. Dubale, W. N. Su and B. J. Hwang, *Nanoscale Horiz.*, 2016, **1**, 243-267.
27. Gurudayal, P. M. Chee, P. P. Boix, H. Ge, Y. N. Fang, J. Barber and L. H. Wong, *ACS Appl. Mater. Interfaces*, 2015, **7**, 6852-6859.
28. Gurudayal, S. Y. Chiam, M. H. Kumar, P. S. Bassi, H. L. Seng, J. Barber and L. H. Wong, *ACS Appl. Mater. Interfaces*, 2014, **6**, 5852-5859.
29. D. W. Kim, S. C. Riha, E. J. DeMarco, A. B. Martinson, O. K. Farha and J. T. Hupp, *ACS Nano*, 2014, **8**, 12199-12207.
30. B. Klahr, S. Gimenez, F. Fabregat-Santiago, J. Bisquert and T. W. Hamann, *Energy Environ. Sci.*, 2012, **5**, 7626-7636.
31. A. Subramanian, A. Annamalai, H. H. Lee, S. H. Choi, J. Ryu, J. H. Park and J. S. Jang, *ACS Appl. Mater. Interfaces*, 2016, **8**, 19428-19437.
32. Z. L. Wang, G. J. Liu, C. M. Ding, Z. Chen, F. X. Zhang, J. Y. Shi and C. Li, *J. Phys. Chem. C*, 2015, **119**, 19607-19612.
33. D. Cibrev, M. Tallarida, C. Das, T. Lana-Villarreal, D. Schmeisser and R. Gomez, *Phys. Chem. Chem. Phys.*, 2017, **19**, 21807-21817.
34. I. A. Cordova, Q. Peng, I. L. Ferrall, A. J. Rieth, P. G. Hoertz and J. T. Glass, *Nanoscale*, 2015, **7**, 12226-12226.
35. E. Courtin, G. Baldinozzi, M. T. Sougrati, L. Stievano, C. Sanchez and C. Laberty-Robert, *J. Mater. Chem. A*, 2014, **2**, 6567-6577.
36. R. Dharmadasa, B. Lavery, I. M. Dharmadasa and T. Druffel, *ACS Appl. Mater. Interfaces*, 2014, **6**, 5034-5040.
37. S. Kment, Z. Hubicka, J. Krysa, D. Sekora, M. Zlamal, J. Olejnicek, M. Cada, P. Ksirova, Z. Remes, P. Schmuki, E. Schubert and R. Zboril, *Appl. Catal., B*, 2015, **165**, 344-350.
38. F. Le Formal, S. R. Pendlebury, M. Cornuz, S. D. Tilley, M. Gratzel and J. R. Durrant, *J. Am. Chem. Soc.*, 2014, **136**, 2564-2574.
39. S. P. Li, P. Zhang, X. F. Song and L. Gao, *Int. J. Hydrogen Energy*, 2014, **39**, 14596-14603.
40. T. F. Li, J. F. He, B. Pena and C. P. Berlinguette, *Angew. Chem. Int. Ed.*, 2016, **55**, 1769-1772.
41. Z. S. Li, J. Y. Feng, S. C. Yan and Z. G. Zou, *Nano Today*, 2015, **10**, 468-486.
42. Y. Liu, J. Li, W. Z. Li, Q. Liu, Y. H. Yang, Y. M. Li and Q. Y. Chen, *Int. J. Hydrogen Energy*, 2015, **40**, 8856-8863.
43. L. Rovelli, S. D. Tilley and K. Sivula, *ACS Appl. Mater. Interfaces*, 2013, **5**, 8018-8024.

44. J. S. Yang, W. H. Lin, C. Y. Lin, B. S. Wang and J. J. Wu, *ACS Appl. Mater. Interfaces*, 2015, **7**, 13314-13321.
45. M. G. Ahmed, I. E. Kretschmer, T. A. Kandiel, A. Y. Ahmed, F. A. Rashwan and D. W. Bahnemann, *ACS Appl. Mater. Interfaces*, 2015, **7**, 24053-24062.
46. Z. W. Fu, T. F. Jiang, L. J. Zhang, B. K. Liu, D. J. Wang, L. L. Wang and T. F. Xie, *J. Mater. Chem. A*, 2014, **2**, 13705-13712.
47. Y. M. Ma, S. R. Pendlebury, A. Reynal, F. Le Formal and J. R. Durrant, *Chem. Sci.*, 2014, **5**, 2964-2973.
48. T. Y. Yang, H. Y. Kang, K. Jin, S. Park, J. H. Lee, U. Sim, H. Y. Jeong, Y. C. Joo and K. T. Nam, *J. Mater. Chem. A*, 2014, **2**, 2297-2305.
49. Q. Ding, F. Meng, C. R. English, M. Caban-Acevedo, M. J. Shearer, D. Liang, A. S. Daniel, R. J. Hamers and S. Jin, *J. Am. Chem. Soc.*, 2014, **136**, 8504-8507.
50. J. W. Moir, E. V. Sackville, U. Hintermair and G. A. Ozin, *J. Phys. Chem. C*, 2016, **120**, 12999-13012.
51. J. J. Wang, Y. L. Hu, R. Toth, G. Fortunato and A. Braun, *J. Mater. Chem. A*, 2016, **4**, 2821-2825.
52. C. M. Ding, J. Y. Shi, Z. L. Wang and C. Li, *ACS Catal.*, 2017, **7**, 675-688.
53. C. Du, J. Wang, X. Liu, J. Yang, K. Cao, Y. W. Wen, R. Chen and B. Shan, *Phys. Chem. Chem. Phys.*, 2017, **19**, 14178-14184.
54. T. H. Wang, H. T. Hung, Y. R. Cheng, M. C. Huang, Y. K. Hsieh and C. F. Wang, *RSC Adv.*, 2016, **6**, 28236-28247.
55. K. M. H. Young and T. W. Hamann, *Chem. Commun.*, 2014, **50**, 8727-8730.
56. X. J. Shi, K. Zhang and J. H. Park, *Int. J. Hydrogen Energy*, 2013, **38**, 12725-12732.
57. B. Eftekharinia, A. Moshaii, A. Dabirian and N. S. Vayghan, *J. Mater. Chem. A*, 2017, **5**, 3412-3424.
58. Q. J. Bu, S. Li, S. Cao, Q. D. Zhao, Y. Chen, D. J. Wang and T. F. Xie, *Dalt. Trans.*, 2017, **46**, 10549-10552.
59. N. D. Carbonare, V. Cristino, S. Berardi, S. Carli, R. Argazzi, S. Caramori, L. Meda, A. Tacca and C. A. Bignozzi, *ChemPhysChem*, 2014, **15**, 1164-1174.
60. H. Schafer, S. Sadaf, L. Walder, K. Kuepper, S. Dinklage, J. Wollschlager, L. Schneider, M. Steinhart, J. Hardege and D. Daum, *Energy Environ. Sci.*, 2015, **8**, 2685-2697.
61. X. N. Huang, L. B. Yang, S. Hao, B. Z. Zheng, L. Yan, F. L. Qu, A. M. Asiri and X. P. Sun, *Inorg. Chem. Front.*, 2017, **4**, 537-540.

62. S. C. Riha, B. M. Klahr, E. C. Tyo, S. Seifert, S. Vajda, M. J. Pellin, T. W. Hamann and A. B. F. Martinson, *ACS Nano*, 2013, **7**, 2396-2405.
63. P. Bornoz, F. F. Abdi, S. D. Tilley, B. Dam, R. van de Krol, M. Graetzel and K. Sivula, *J. Phys. Chem. C*, 2014, **118**, 16959-16966.
64. F. F. Abdi and R. van de Krol, *J. Phys. Chem. C*, 2012, **116**, 9398-9404.
65. Y. Ma, F. Le Formal, A. Kafizas, S. R. Pendlebury and J. R. Durrant, *J. Mater. Chem. A*, 2015, **3**, 20649-20657.
66. Y. M. Ma, A. Kafizas, S. R. Pendlebury, F. Le Formal and J. R. Durrant, *Adv. Funct. Mater.*, 2016, **26**, 4951-4960.
67. S. K. Pilli, T. E. Furtak, L. D. Brown, T. G. Deutsch, J. A. Turner and A. M. Herring, *Energy Environ. Sci.*, 2011, **4**, 5028-5034.
68. W. T. Qiu, Y. C. Huang, S. T. Tang, H. B. Ji and Y. X. Tong, *J. Phys. Chem. C*, 2017, **121**, 17150-17159.
69. A. Dabirian and R. van de Krol, *Chem. Mater.*, 2015, **27**, 708-715.
70. G. J. Liu, J. Y. Shi, F. X. Zhang, Z. Chen, J. F. Han, C. M. Ding, S. S. Chen, Z. L. Wang, H. X. Han and C. Li, *Angew. Chem. Int. Ed.*, 2014, **53**, 7295-7299.
71. G. J. Liu, S. Ye, P. L. Yan, F. Q. Xiong, P. Fu, Z. L. Wang, Z. Chen, J. Y. Shi and C. Li, *Energy Environ. Sci.*, 2016, **9**, 1327-1334.
72. M. Bledowski, L. D. Wang, S. Neubert, D. Mitoraj and R. Beranek, *J. Phys. Chem. C*, 2014, **118**, 18951-18961.
73. K. L. Materna, J. B. Jiang, K. P. Regan, C. A. Schmittenmaer, R. H. Crabtree and G. W. Brudvig, *ChemSusChem*, 2017, **10**, 4526-4534.
74. G. Z. Xu, Z. Xu, Z. Shi, L. Pei, S. C. Yan, Z. B. Gu and Z. G. Zou, *ChemSusChem*, 2017, **10**, 2897-2903.
75. E. Pastor, F. Le Formal, M. T. Mayer, S. D. Tilley, L. Francas, C. A. Mesa, M. Gratzel and J. R. Durrant, *Nat. Commun.*, 2017, **8**.
76. A. Sarkar, K. Karmakar and G. G. Khan, *J. Phys. Chem. C*, 2017, **121**, 25705-25717.
77. F. A. L. Laskowski, M. R. Nellist, R. Venkatkarthick and S. W. Boettcher, *Energy Environ. Sci.*, 2017, **10**, 570-579.
78. K. Sun, N. L. Ritzert, J. John, H. Tan, W. G. Hale, J. Jiang, I. Moreno-Hernandez, K. M. Papadantonakis, T. P. Moffat and B. S. Brunshwig, *Sustainable Energy & Fuels*, 2018, Advance online publication. DOI: 10.1039/c1037se00583k.
79. A. M. Cowley and S. M. Sze, *J. Appl. Phys.*, 1965, **36**, 3212-3220.
80. N. Konofaos, I. P. McClean and C. B. Thomas, *Phys. Status Solidi A*, 1997, **161**, 111-123.

81. D. Monllor-Satoca, M. Bartsch, C. Fabrega, A. Genc, S. Reinhard, T. Andreu, J. Arbiol, M. Niederberger and J. R. Morante, *Energy Environ. Sci.*, 2015, **8**, 3242-3254.
82. P. Sahay, M. Shamsuddin and R. Srivastava, *Microelectron. J.*, 1992, **23**, 625-632.
83. A. N. Saxena, *Surf. Sci.*, 1969, **13**, 151-171.
84. Q. Shi, S. Murcia-López, P. Tang, C. Flox, J. R. Morante, Z. Bian, H. Wang and T. Andreu, *ACS Catal.*, 2018, Advance online publication. DOI: 10.1021/acscatal.1027b04277.
85. F. D. Lin and S. W. Boettcher, *Nat. Mater.*, 2014, **13**, 81-86.
86. J. Qiu, H. Hajibabaei, M. R. Nellist, F. A. Laskowski, T. W. Hamann and S. W. Boettcher, *ACS Cent. Sci.*, 2017, **3**, 1015-1025.
87. M. S. Burke, L. J. Enman, A. S. Batchellor, S. H. Zou and S. W. Boettcher, *Chem. Mater.*, 2015, **27**, 7549-7558.
88. A. M. Smith, L. Trotochaud, M. S. Burke and S. W. Boettcher, *Chem. Commun.*, 2015, **51**, 5261-5263.
89. L. Trotochaud, S. L. Young, J. K. Ranney and S. W. Boettcher, *J. Am. Chem. Soc.*, 2014, **136**, 6744-6753.
90. Y. M. Ma, C. A. Mesa, E. Pastor, A. Kafizas, L. Francas, F. Le Formal, S. R. Pendlebury and J. R. Durrant, *ACS Energy Lett.*, 2016, **1**, 618-623.
91. K. Sivula, *J. Phys. Chem. Lett.*, 2013, **4**, 1624-1633.
92. D. K. Lee and K. S. Choi, *Nat. Energy*, 2018, **3**, 53-60.
93. F. M. Toma, J. K. Cooper, V. Kunzelmann, M. T. McDowell, J. Yu, D. M. Larson, N. J. Borys, C. Abelyan, J. W. Beeman, K. M. Yu, J. H. Yang, L. Chen, M. R. Shaner, J. Spurgeon, F. A. Houle, K. A. Persson and I. D. Sharp, *Nat. Commun.*, 2016, **7**.
94. G. J. Ai, R. Mo, H. X. Li and J. X. Zhong, *Nanoscale*, 2015, **7**, 6722-6728.
95. L. D. Wang, D. Mitoraj, S. Turner, O. V. Khavryuchenko, T. Jacob, R. K. Hocking and R. Beranek, *ACS Catal.*, 2017, **7**, 4759-4767.
96. D. D. Xu, Z. W. Fu, D. J. Wang, Y. H. Lin, Y. J. Sun, D. D. Meng and T. F. Xie, *Phys. Chem. Chem. Phys.*, 2015, **17**, 23924-23930.

TOC graphic



Dual-working-electrode photoelectrochemistry experiments reveal how the most-prominent photocurrent transients are associated with catalyst oxidation/reduction.